RSC Advances

ROYAL SOCIETY OF CHEMISTRY

www.rsc.org/advances

One step hydrothermal synthesis of Mn_3O_4/graphene composites with great electrochemical properties for lithium-ion batteries

YuRong Ren [a, *], JiaWei Wang [a], XiaoBing Huang [b], Bo Yang [a] and JianNing Ding [a,*].

a School of Materials and Engineering, Changzhou University, Changzhou 213164, C hina

b College of Chemistry and Chemical Engineering, Hunan University of Arts and Scie nce, Changde 415000, China

Abstract: The fabrication and electrochemical performance of Mn_3O_4/graphene composites are discussed in this work. The main procedures of reaction consist of two parts: one is the formation of Mn_3O_4 particles; the other is the reduction of graphite oxide to graphene. The chemicals, $MnCl_2$•$4H_2O$ and $NaBH_4$ are employed as a manganese source and a reduction regent, respectively. During the formation of Mn_3O_4 particles, NH_3 is added to the reaction system, directly, which simplifies the hydrolysis of amide, and the surfactant, polyvinylpyrrolidone (PVP), is used to ensure great dispersion and size-controlled formation of Mn_3O_4 particles. The resulting materials are characterized by XRD, SEM, HRTEM, FT-IR, Raman and XPS. Mn_3O_4 particles dispersing on the surface of graphene have the average diameter of ca.30 nm. The materials deliver a stable reversible capacity of ca.500 mAh/g at a current density of 60 mA/g even after 100 cycles. The reversible capacity of samples coating with

* Corresponding authors: Tel: +86 18761162096
E-mail address: ryrchem@cczu.edu.cn (Y.R. Ren)
* Corresponding authors: Tel: +86 18810891227
E-mail address: ryrchem@163.com (J.N. Ding)

graphene is much better than that of pure materials.

Keywords: hydrothermal synthesis; Mn_3O_4/graphene; polyvinylpyrrolidone; anode materials; Lithium-ion battery;

1. Introduction

Energy, as a significant material basis contributing to the development of human society, has various employments in our daily lives. How to recycle and store it? Energy storage devices, such as supercapacitor [1], redox flow battery [2], sodium-sulfur cell and lithium-ion battery [3], are the solution to this matter. But that how to improve the cycling stability and enhance the capacity of energy storage devices becomes another question needs to be solved. It is found that, as an important part of these energy storage devices, electrode materials are the momentous factors that influence their electrochemical performances. In some previous researches, various materials were utilized to improve the properties of these devices. Transition metal oxides [4], [5], carbon materials and conducting polymers [6～9] all have the great dedications to the progress of these devices, in particular to the lithium-ion battery.

Transition metal oxides materials, like Fe_3O_4 [10], ZnO [11], CuO [12] and Mn_3O_4 [13], were used as anode materials for lithium-ion battery research in some previous works. Among them, Mn_3O_4 materials known to have a normal spinel structure with tetragonal distortion elongated along the c-axis because of Jahn–Teller effect on the Mn^{3+} ion, is one of the most attractive materials employed as an anode electrode for lithium-ion battery due to the easy availability of manganese, its low

cost, environmentally benign and a high theoretical specific capacity (approximately 936 mAh/g). However, the shortcomings of high electrical resistance, poor electrochemical reversibility and low electrical conductivity (~10^{-7}—10^{-8} S/cm), et al [14], [15], limit its practical application in anode materials for lithium-ion battery. To overcome these disadvantages, many different methods were taken advantages of in the prior studies. For example, adding the surfactants [16], doping Mn_3O_4 with Co [17], [18], synthesizing nanosized Mn_3O_4 anode materials [19], coating Mn_3O_4 with carbon materials, et al, are all the effective approaches to polishing up the electrochemical properties of Mn_3O_4 materials. In our study, the method, coating Mn_3O_4 with carbon materials, was operated as examples.

Carbon materials, such as dense and long carbon nanotube arrays [20], the activated mesocarbon microbead [21], uniform carbon layer [22], ball-milled graphite [23], graphene [24], [25], et al, combined with Mn_3O_4 nanoparticles perform the improved the capacity and the stability for lithium ion battery. Especially, graphene, because of its great electrochemical properties (the theoretical specific capacity is ca.744 mAh/g), excellent flexibility and large specific surface area, is described as the best selection of being the conductive matrix and the support of sediments nanoparticles for anode materials [15]. Mn_3O_4/graphene nanocomposites can be synthesized by various methods, and present great electrochemical performances in many studies. For instant, Liu [26], et al, synthesized Mn_3O_4/graphene nanocomposites by microwave-assisted hydrothermal method; Park [27], et al, prepared the samples by one-step sonochemical method; Nam [28], et al, synthesized

the samples, Mn_3O_4/graphene nanocomposites, by an in-situ transformation method. In our experiment, a one-pot hydrothermal synthesis of Mn_3O_4/graphene nanocomposites was carried out. The main procedures of reaction consist of two parts: one is the formation of Mn_3O_4 nanoparticles; the other is the reduction of graphite oxide to graphene. The graphite oxides powders used in this study were prepared by a modified hummer's method. In addition, the reactions neither produce any toxic byproducts nor cost much reaction-energy. Meanwhile, the one-step accomplishment for the oxidation of Mn^{2+} and the reduction of graphite oxide to graphene economized the reaction-time as well as simplified the reaction-procedures.

The performances of two samples, Mn_3O_4 and Mn_3O_4/graphene were measured by some characterizations and electrochemical tests. It comes to that the specific capacity and cycling stability of lithium-ion battery has a great improvement by coating the anode materials with carbon materials. To the best of our knowledge, combing transition metal oxide with carbon materials is indeed the most feasible method to achieve the improvement of performances in practices.

2. Experiment details

2.1. Chemicals

Commercial graphite powders (C.P, 98%, sinopharm chemical reagent Co., Ltd); Sulfric acid (H_2SO_4, A.R., 95%～98%, Beijing Chemical Works); Sodium nitrate ($NaNO_3$, A.R., 99%, Beijing Yili Fing Chemical Co., Ltd.); Potassium permanganate ($KMnO_4$,A.R., 99.5%, Beijing Chemical Works); Hydrogen peroxide (30%, H_2O_2, A.R., >30%, Beijing Chemical Works); Hydrochloric acid (HCl, A.R.， 36%,

Beijing Chemical Works); Manganese chloride ($MnCl_2$•$4H_20$, A.R., ≥99.0%, Beijing Chemical Works); Ammonia solution (NH_3•H_2O, A.R., 25%, Beijing Chemical Works); Polyvinylpyrrolidone (PVP, the molecular weight=40000 (avg.), Beijing Kebio Bio-Technique Co., Ltd.); Sodium borohydride ($NaBH_4$, A.R., ≥98.0%, Tianjin Fuchen Chemical Reagents Factory).

2.2. Sample preparation

2.2.1 Preparation of graphite oxide (GO)

Graphite oxide used in this experiment was prepared by a modified Hummer's method [29], [30]. 1.5 g of $NaNO_3$ powder was added into the 69 ml of H_2SO_4 solution in a three-necked flask with stirring in the ice-water-bath. When the powder dissolved completely, 3 g of graphite powder and 9 g of $KMnO_4$ were added into the mixture with stirring for 10 min. Then, the ice-water bath was removed and the temperature was kept at 35 □ for 2 h by the water-bath. 137 ml of the deionized water was injected into the resulting solution at 95 □. The temperature was maintained at 95 □ for 15 min. The resulting solution was diluted to 420 ml with warm-water and 10 ml of H_2O_2 was added into the solution. Then, the solution became yellow. The products were filtered and washed once with 330 ml of hydrochloric acid solution and three times with distilled water. Finally, the samples were dried for 24 h under an atmosphere at 45 □.

2.2.2 Preparation of graphene and Mn_3O_4/graphene (MGC)

Firstly, 40 mg of GO powder was added into 30 ml of the deionized water with stirring for 10 min and ultrasonic irradiation for 2 h. Next, 2 mmol of $MnCl_2·4H_2O$

and 1.2 g of PVP were dissolved in 10 ml of the deionized water with stirring for 3 h. Then, 0.8 ml of NH_3 was inject into the resulting solution with a pipette with stirring for 1 h. Afterwards, 20 mg of $NaBH_4$ was added into the previous solution with stirring for 10 min. Finally, the resulting mixture was aged in an autoclave at 140 □ for 8 h. After it cooled to room temperature, the samples were filtered and washed three times with distilled water and absolute ethyl alcohol, respectively. The Mn_3O_4/graphene nanoparticles were precipitated by drying at 80 □ for 4 h. For comparison, sample of pure graphene was also prepared using a similar method.

2.2.3 Preparation of Mn_3O_4

The preparation of Mn_3O_4 nanoparticles was similar to the preparation of Mn_3O_4/graphene nanoparticles except the first step. GO powder was needless in this preparation.

2.3 Characterization of the samples

The structure and the phases of the samples were characterized by X-ray diffraction (XRD, Bruker D8 advance with Cu K_α, λ = 1.5418 Å, 40 KV, 40 mA). The morphology of the samples was investigated by transmission electron microscopy (TEM, Hitachi H7650B, 120 kV), high resolution transmission electron microscopy (HRTEM, TECNAI G^2 20, 200 kV) and scanning electron microscopy (SEM, JEOL JSM-6360LA, 120 kV). The morphology of pristine graphene was investigated by transmission electron microscopy (TEM, JEOL JEM-2100). The surface chemical environments of the samples were analyzed by X-ray photoelectron spectroscopy (XPS, 250XI X-ray photoelectron spectrometer with an Al/Mg-Ka/Al X-ray source).

The content of graphene was measured by thermogravimetric analysis (TGA, NETZSCH TG 209F1 Libra) from room temperature to 850 ℃ at a heating rate of 10 ℃/min under O_2. Raman spectra were measured on a RM2000 Raman Spectrometer (Renishaw, British). FT-IR Spectra were tested by a NICOLET 560 Fourier transform infrared spectrophotometer.

2.4 Electrochemical analysis

The working electrode was prepared by mixing 80 wt% of the samples as the active material, 10 wt% Super P as a conductive additive, and 10 wt% sodium carboxymethyl cellulose (CMC) as a binder of the total electrode mass. The three components were mixed with the deionized water as the solvent to produce slurry. It was uniformly loaded on a Cu foil with a doctor blade as a current collector and compressed to prepare a film-type electrode. The sample was cut into circular electrodes and dried for 12 h under vacuum at 105 □. The cells were assembled in an Ar-filled glovebox (ZKX2, Nanjing University Instrument Factory) with lithium foil as the anode, and a solution of 1.0 M $LiPF_6$ dissolved in 1:1 (v/v) EC/DEC as the electrolyte. All electrochemical measurements were carried out on a CT2001A Land battery testing system in the potential range from 0.01 V to 3 V (vs. Li^+/Li). The AC impedance data were recorded in the frequency range 10^{-2} Hz to 10^5 Hz using CHI760E electrochemical station (Shanghai Chenhua).

3. Results and discussion

3.1. Characterizations

3.1.1. Structure and morphology analysis

To study crystalline nature of prepared samples, the XRD pattern was recorded in the 2θ range 20～100º and HRTEM was brought to bear.

The crystalline structures of Mn_3O_4/graphene composite materials were examined by XRD analysis in Fig.1. The main characteristic peaks of XRD curve (Fig.1d) get a great agreement with JCPDS Card (NO. 80-0382) that meant to be the tetragonal structure of Mn_3O_4. In accordance with the formula: $1/d^2 = (h^2 + k^2)/a^2 + l^2/c^2$, where d is interplanar spacing of the samples, (h k l) is the symbol of indicates of crystal face, 'a' and 'c' are the lattice parameters of tetragonal structure of Mn_3O_4, the actual value of lattice parameters can be figure out (average size: a = 5.742 Å, c = 9.448 Å). And the peak at ca.24° is indexed to the graphitic planes (002) of graphene nanosheets [25]. Observing the XRD pattern of GO and rGO (Fig.1d), the characteristic stacking peak shifted from ca.10° to ca.24°, which indicates that GO has been converted into graphene with the help of reductant and hydrothermal treatment. Moreover, from the HRTEM images of Mn_3O_4/graphene nanocomposites (Fig.1e), it can be observed that Mn_3O_4 nanoparticles are composed of nanocrystal lines with a lattice spacing of about 0.464 nm. Contracting with dates obtained from XRD analysis, it is (101) plane of the hausmannite structure. Meanwhile, the polycrystalline nature of Mn_3O_4 nanoparticles can be demonstrated from the SAED patterns (Fig.1f).

The TEM images of pristine graphene show that the graphene we prepared gets the wrinkled morphology and has the structure of multilayers (Fig.1g). After the introduction of Mn_3O_4 particles, the electrochemically active surface area of graphene

would be enlarged with the anchored Mn_3O_4 nanoparticles on the surface of the graphene platelets. The Mn_3O_4 nanoparticles are dispersed on the surface of graphene evenly (Fig.1a, 1c). The size of these particles is approximately 30 nm (Fig.1b), and this value is close to the outcome (about 27 nm) calculated by the Scherer's relation of XRD: $D = Kl/b\cos q$ where D is grain size of the Mn_3O_4 nanoparticles, K is the fullwidth at halfmaximumintensity (*FWHM*) in radians, and q is the Bragg angle.

The morphology of the samples obtained by FE-SEM investigation is shown in Fig.2. In Fig.2a (scale bar = 1 μm) and Fig.2b (scale bar = 100 nm), the substrate surface is covered uniformly with prism-like Mn_3O_4 nanomaterials. These prisms are interlocked with each other or aggregated, and the diameter of the cross section for these prism is approximately 100 nm and the length of them is 700 nm～1100 nm. Apart from these prisms, some sphere-like and cluster-like nanoparticles can be observed as well due to the overgrowth of samples.

In Fig.2c (scale bar = 100 nm) and Fig.2d (scale bar = 100 nm), Mn_3O_4 nanoparticles are closely attached and highly dispersed on the surface of graphene. However, perhaps because of the overdose of Mn_3O_4, some extra Mn_3O_4 nanoparticles not absorbed by graphene are found in Fig.2c (the part marked by black circle). And the gain size of Mn_3O_4 absorbed on the surface of graphene mainly distributes in the range of 30 nm to 70 nm (Fig.2e).

3.1.2 FT-IR study

IR spectrum of the samples synthesized is delineated in Fig.3a. Functional groups that the samples contain can be analyzed on the basis of the position of the

peaks. The peak at ca.3428 cm^{-1} symbolizes the existence of "OH" groups and the peak at ca.1730 cm^{-1} illustrates the presence of "C=O" groups. Comparing the peaks in the same position of 3428 cm^{-1} and 1730 cm^{-1}, respectively, the peak of Mn_3O_4/graphene becomes less intensive than that of graphite oxide. Even the peak at ca.1730 cm^{-1} is invisible in the above dotted line. It's supposed that when graphite oxide was reduced to graphene, these functional groups at the surface of the samples were substituted by "C=C" groups and Mn_3O_4 molecules, and it is the reason why the peaks of "COOH" groups and "-C-O-C-"groups within the range of 1500 cm^{-1} to 1000 cm^{-1} are become weaker as well. From the foregoing analysis, although there are still a few oxygen molecules being left over, the reduction effect of $NaBH_4$ is satisfactory. And the peak at ca.1634 cm^{-1} as marked in Fig.3a signifies that there are some "C=C" groups in the samples. This is specific structure of graphene, meaning the SP^2 hybridization of carbon structures. In addition, two obvious absorption bands, which are related with the coupling mode between Mn-O stretching modes of tetrahedral and octahedral sites, can be found at ca.500 cm^{-1} in the curve of Mn_3O_4/graphene materials [31]. Therefore, FT-IR results provide further evidence of the formation of Mn_3O_4 nanoparticles and the reduction of graphite oxide to graphene.

3.1.3 Raman test

Fig.3b exhibits the Raman curves of graphite oxide, graphene and Mn_3O_4/graphene. The only difference found in the curves is a small peak in Raman shift of ca.655 cm^{-1} which reflects the existence of Mn_3O_4 nanoparticles. Other peaks are the characteristic Raman shifts of graphene. The peak at ca.1350 cm^{-1} called

D-peak, representing the lattice defects of carbon atom, reflected the randomness of graphite layers and the peak at ca.1595 cm^{-1} called G-peak, delegating SP^2 hybridization of carbon structures, suggested the symmetry and the crystallinity of graphene. And more intensive the G-peak is, more excellent the quality of graphene is, but the D-peak is on the contrary. In theory, if the prepared graphene is unilaminar, there should be only one 2D-peak originating from the inelastic scattering of two double-phonons in Raman curve and the intensity of 2D-peak ought to be higher than G-peak. According to Fig.3b, it's obvious that graphene we prepared is multilayered, and this result can be confirmed by TEM analysis as well (Fig.1 (g)).

3.1.4 Composition analysis

The elemental compositions of the sample were examined by XPS analysis. Fig.4a shows a typical survey XPS spectrum of Mn_3O_4/graphene nanoparticles. All of the elements consist of five contributions of manganese species (3p, 3s, 2p3/2, 2p1/2), carbon species (1s), nitrogen species (1s), oxide species (1s) and fluorine species. To do a deeper analysis, the XPS species for the C1s region exhibited in fig.4b are made up of three dedications at ca.284.84, 285.94 and 287.93 eV, which corresponding to carbon sp2 bonding (C-C), epoxy/hydroxyl groups (C-O), and carbonyl/carboxyl groups (O-C=O/C=O), respectively. By accessing to some literature [17], it is happened that the peaks indicating epoxide/hydroxyl groups (C-O), and carbonyl/carboxyl groups (C=O) should have become extensive, and the peak associated with "C-C" bond should have been predominant, while the graphite oxide was reduced to graphene completely. However, the intensity of peak signifying "C-O"

bond, observed in fig.4b, is feckly as intensive as "C-C" bond. So, the result of the reducing agent we employed is unsatisfactory. The manganese oxidation state is affirmed by the analysis of Mn (3s, 2p) peak splitting width. As shown in Fig.4c, The splitting width of Mn3s is ca.5.9 eV, which has a well agreement with other earlier articles [32] on Mn_3O_4 as well as the splitting width of Mn3s (ca.12.4 eV). So, it is proved that resultant of the reaction is indeed Mn_3O_4/graphene.To study the real mass content of Mn_3O_4 and graphene in MGC, TGA analysis was taken into advantage. The mass loss beginning from 150℃ to 400℃ indicates the decomposition of graphene into CO_2 and H_2O [33]. To avoid the interference of mass variation of Mn_3O_4, pristine Mn_3O_4 was measured under the same circumstances. And the mass-loss of pristine Mn_3O_4 from 150℃ to 400℃ is attributed to decomposition of PVP. The mass content of Mn_3O_4 and graphene are estimated to be 86.53% and 13.47% (Fig.4e, Fig.4f), respectively. While reaching above 500℃, the mass of samples does not undergo any distinct degradation, which indicates the thermostability of Mn_3O_4. On the basis of these dates and the theoretical specific capacity of each composition, the theoretical specific capacity of sample can be figured out with the formula. Taking this sample as an example, sum = 744 mAh/g × 13.47% + 936 mAh/g × 86.53%=910.14 mAh/g.

3.2 Electrochemical measurement

The fig.5a displays the comparison of discharge/charge capacity between Mn_3O_4 and Mn_3O_4/graphene electrode at the current density of 60 mA/g for 100 times. In initial cycle, the discharge and charge capacity of Mn_3O_4 electrode is ca.291.1 mAh/g

and ca.130.4 mAh/g, and that of Mn_3O_4/graphene electrode is ca.897.2 mAh/g and ca.456.4 mAh/g, respectively. It is interesting to note that the initial discharge capacity of Mn_3O_4/graphene is much lower than the theoretical value calculated by TGA analysis (910.14 mAh/g). This phenomenon is ascribed to the incomplete utilization of active materials. Moreover, for Mn_3O_4 and Mn_3O_4/graphene electrode, the voltage range of 1.3 to 0.3 V both has an inclined curve (fig.5b). It is caused by the formation of very thick solid electrolyte interface (SEI) film on the surface of the electrodes. However, the capacity efficiency of Mn_3O_4/graphene electrode (ca.50%) is much higher than that of Mn_3O_4 electrode (ca.45%). The unsatisfactory of the initial charge-discharge might be due to the reaction between the electrolyte and the oxygen-containing groups that the samples have.

In the first 30 cycles, the capacity of Mn_3O_4/graphene and pristine Mn_3O_4 electrodes are both not stable. The ups and downs of capacity of Mn_3O_4/graphene electrodes might result from the scaling of overdose Mn_3O_4 particles (marked in Fig.2c) which are not coated with graphene. With the cycling going on, because of gradual stability of material structure which owns to the supporting function of graphene, the capacity of Mn_3O_4/graphene electrode can maintains at a level of ca.500 mAh/g after 30 cycles, but the capacity of Mn_3O_4 electrode shows a little attenuation to ca.140 mAh/g after 50 cycles (without the support of graphene, the pristine Mn_3O_4 electrodes undergo a large volume change in the process of lithium insertion and escape, resulting in disintegration of the crystals and loss of the connection between

the electrode materials and the current collector [34]). All of these illustrate that the cycling performance of samples has an optimization after coated with graphene.

The rate capacity of samples is measured at the current density of 60, 250, 500, 750 mA/g, respectively (Fig.5c). The capacities of Mn_3O_4 electrode are ca.150, ca.110, ca.60, ca.50 mAh/g, respectively, and that of Mn_3O_4/graphene electrode are ca.450, ca.320, ca.250, ca.220 mAh/g, respectively. The capacity of Mn_3O_4/graphene at the current density of 60 mA/g is not stable as well as pristine Mn_3O_4, and this phenomenon is ascribed to the instability of material structure in the initial several cycles (the scaling of overdose Mn_3O_4 particles in MGC or the large volume change of pristine Mn_3O_4). However, with the cycling going on, the capacity of samples is stable even at the higher current density because of gradual stability of material structure. Meanwhile, the capacity of Mn_3O_4/graphene is always much higher than that of pristine Mn_3O_4. It is being coated with graphene that enhances the capacity of samples.

Fig.6 shows Nyquist plots of Mn_3O_4 and Mn_3O_4/graphene electrodes obtained at the current density of 60 mA/g after different cycling number.

The Nyquist plots of Mn_3O_4 and Mn_3O_4/graphene electrode consist of two parts: a semicircle in the high frequency region and a vertically linear spike in the low frequency region, which are associated with the process of the charge transfer in the electron / ion conductive junction and the diffusion of lithium ion through the active material, respectively(Fig.6a, Fig.6b). From the figures, it is obviously that with the increasing in cycling number, the electrical resistance of the charge transfer become

smaller, and the diffusion coefficient get a little increasing. It may have something to do with the activation of samples. But in the partial enlargement (Fig.6b), it is observed that two semicircles show up in the high frequency region, which is due to the formation of SEI film. And the absence of this semicircle in other curves may result from that the electrical resistance of SEI film is not big enough to be observed.

The electrochemical parameters are obtained by the fitting of equivalent circuit (fig.6c). And the raw dates and fitting dates of two samples got after 10 cycles are exhibited in fig.6d and fig.6e, respectively.

The common equivalent circuit of lithium ion battery is shown as fig.7 [35], [36]. And in this article, the Constant Phase Element (CPE_1) is employed to replace the capacitor.

$$Z_{\mathrm{CPE1}} = [T \times (j \times w)\text{^}p]^{-1} \quad (1)$$

$$Z_{\mathrm{W1}} = R \times \mathrm{ctnh}[(j \times T \times w)\text{^}p]/\ (j \times T \times w)\text{^}p \quad (2)$$

Table.1 Electrochemical parameters of the samples

Sample	Mn_3O_4	MGC
R_s (Ω)	2.38	2.074
CPE_1-T ($\Omega^{-1} \times cm^{-2} \times s\text{^}P$)	0.00011035	0.00021644
CPE_1-P	0.69288	0.51166
R_1 (Ω)	223.1	96.88
W_1-R (Ω)	27.5	4572
W_1-T (s)	0.0010632	71.89
W_1-P	0.28607	0.58608

Observing the date showing in Table.1, the electrochemical resistance of porous diaphragm, electrolyte, et al (R_s) and charge transfer (R_1) of Mn_3O_4 electrode are both higher than that of Mn_3O_4/graphene electrode. Open Circuit Terminus (W_1) is defined by three values: W_1-R, W_1-T and W_1-P. W_1-T = L^2 / D, where L is the effective diffusion thickness and D is the effective diffusion coefficient of the particle. According to the slope of the vertically linear spike in the low frequency region, two samples have the similar effective diffusion coefficient, but the gap between the values of W_1-T is big. In association with the formula, the effective diffusion thickness of Mn_3O_4/graphene electrode is much bigger than that of Mn_3O_4 electrode, and it might be one reason why the capacity of Mn_3O_4/graphene electrode is much higher than that of Mn_3O_4 electrode. And the high electrical resistance of Mn_3O_4 electrode influences the transfer velocity of lithium ion, which leads to the poor rate capacity of it as well. So Mn_3O_4/graphene electrode obtains the much greater electrochemical properties than Mn_3O_4 electrode.

3.3 The formation mechanism of the samples [37], [38], [39]

In this synthesis, Mn_3O_4 nanoparticles were grown on graphene nanosheets by a one-pot hydrothermal method to prepare Mn_3O_4/graphene nanocomposite materials.

For this procedure, firstly, Graphite oxide prepared by a modified improved hummers' method provided much many oxygen-containing functional groups which are on the surface of graphite oxide for the attachment of Mn^{2+} ions via electrostatic interactions. In the reaction, these Mn^{2+} ions were oxidized with oxygen contained in a functional group on the surface of graphite oxide.

With the stirring under the room-temperature, free Mn^{2+} ions were released from the stable precursor. Then, ammine complexes of $Mn(NH_3)_n^{2+}$ (n = 1～4) were formed when NH_3 (aq) was added into the solution to react with Mn^{2+} ions:

$$Mn^{2+} + nNH_3 \rightleftarrows Mn(NH_3)_n^{2+} \quad (3)$$

The intermediate products, $Mn(NH_3)_n^{2+}$ (n = 1～4), were unstable on the reaction condition (due to the addition of NH_3 (aq), the solution is alkalescent.), so the following reaction occurred:

$$Mn(NH_3)_n^{2+} \rightleftarrows Mn^{2+} + nNH_3 \quad (4)$$

Finally, oxidation of Mn^{2+} to Mn^{3+} takes place as

$$6Mn^{2+} + O_2 + 12OH^- \rightleftarrows 2Mn_3O_4 + 6H_2O \quad (5)$$

And the reagent, $NaBH_4$, was employed as the reaction of graphite oxide. While, PVP reagent was added to ensure great dispersion and size-controlled formation of the samples which would avoid the excessive size of Mn_3O_4.

4. Conclusion

In summary, Mn_3O_4/graphene nanocomposites are fabricated by a one-pot hydrothermal method with $MnCl_2$•$4H_2O$ as manganese donor and $NaBH_4$ as the reduction of graphene oxide to graphene, successfully and the chemical, PVP, indeed plays a good role of control agent that ensures the great dispersion and size-controlled formation of Mn_3O_4 on the surface of graphene. The electrochemical performances of samples get a great improvement after being coated with graphene.

For further optimization, doping with other metal elements is a valuable approach to attempt. And the initial charge-discharge efficiency of the samples leaves

much to be desired, being coated with some other polymer may be effective on improving the performances of the materials.

Conflict of interest

The authors declare that there is no conflict of interest.

Acknowledgments

This study was supported by National Natural Science Foundation of China (51304077 and 51374175), Science and Technology Department of Science and Technology of Project in Jiangsu Province (BY2014037-31), the Privileged Development Program of Jiangsu High Education on New energy material science and engineering, the Opening Project of State Key Laboratory of Alternate Electrical Power System with Renewable Energy Sources (Grant No. LAPS15001), Material Corrosion and Protection Key Laboratory of Sichuan province (2014CL15) are acknowledged.

Reference

[1] J. M. Miller, New Ultracapacitor Applications, Institution of Engineering & Technology, Steven age, 2011.

[2] R. Badrinarayanan, J. Y. Zhao, K. J. Tseng and S. K. Maria, *J. Power Sources*, 2014, **270**, 576–586.

[3] T. R. Crompton, Battery Reference Book, Science Direct, Newnes, 2000.

[4] S. Komaba, T. Tsuchikawa, A. Ogata, N. Yabuuchi, D. Nakagawa and M. Tomita, *Electrochim. Acta*, 2012, **59**, 455–463.

[5] W. F. Zhang, F. Liu, Q. Q. Li, Q. L. Shou, J. P. Cheng, L. Zhang, B. J. Nelson and

X. B. Zhang, *Phys. Chem. Chem. Phys.*, 2012, **14**, 16331–16337.

[6] S. Sahoo, G. Karthikeyan, G. C. Nayak and C. K. Das, *Synth. Met.*, 2011, **161**, 1713–1719.

[7] D. C. Zhang, X. Zhang, Y. Chen, P. Yu, C. H. Wang and Y. W. Ma, *J. Power Sources*, 2011, **196**, 5990–5996.

[8] C. H. Xu, J. Sun and L. Gao, *J. Mater. Chem.*, 2011, **21**, 11253–11258.

[9] P. Si, S. J. Ding, X. W. Lou(David) and D. H. Kim, *RSC Advances*, 2011, **1**, 1271–1278.

[10] A. P. Hu, X. H. Chen, Q. L. Tang and B. Zeng, *Ceram. Int.*, 2014, **40**, 14713–14725.

[11] E. R. Ezeigwe, M. T. T. Tan, P. S. Khiew and C. W. Siong, *Ceram. Int.*, 2015, **41**, 715–724.

[12] J. Y. Xiang, J. P. Tu, L. Zhang, Y. Zhou, X. L. Wang and S. J. Shi, *J. Power Sources*, 2010, **195**, 313–319.

[13] S. H. Guo, M. Zhang, G. N. Zhang, L. Zheng, L. P. Kang and Z. H. Liu, *Powder Technol.*, 2012, **228**, 371–376.

[14] J. Y. Qu, F. Gao, Q. Zhou, Z. Y. Wang, H. Hu, B. B. Li, W. B. Wan, X. Z. Wang and J. S. Qiu, *Nanoscale*, 2013, **5**, 2999–3005.

[15] L. E. F. F. Torres, S. Roche and J. C. Charlier, Introduction to Graphene-Based Nanomaterials-From Electronic structure to Quantum Transport, Cambridge University Press, New York, 2014.

[16] Y. F. Lee, K. H. Chang, C. C. Hu and Y. H. Chu, *J. Power Sources*, 2012, **206**,

469–475.

[17] J. Z. Wang, N. Du, H. Wu, H. Zhang, J. X. Yu and D. R. Yang, *J. Power Sources*, 2013, **222**, 32–37.

[18] Z. Q. Li, N. N. Liu, X. K. Wang, C. B. Wang, Y. X. Qi and L. W. Yin, *J. Mater. Chem.*, 2012, **22**, 16640–16648.

[19] J. Z. Wang, N. Du, H. Wu, H. Zhang, J. X. Yu and D. R. Yang, *J. Power Sources*, 2013, **222**, 32–37.

[20] X. W. Cui, F. P. Hu, W. F. Wei and W. X. Chen, *Carbon*, 2011, **49**, 1225–1234.

[21] H. Q. Wang, Z. S. Li, J. H. Yang, Q. Y. Li and X. X. Zhong, *J. Power Sources*, 2009, **194**, 1218–1221.

[22] C. B. Wang, L. W. Yin, D. Xiang and Y. X. Qi, *ACS Appl. Mater. Interfaces*, 2012, **4**, 1636−1642.

[23] J. Y. Cao, Y. M. Wang, Y. Zhou, D. C. Jia, J. H. Ouyang and L. X. Guo, *J. Electroanal. Chem.*, 2012, **682**, 23–28.

[24] S. H. Yang, X. F. Song, P. Zhang and L. Gao, *J. Mater. Chem.*, 2013, **1**, 14162–14169.

[25] X. Zhang, X. Z. Sun, Y. Chen, D. C. Zhang and Y. W. Ma, *Mater. Lett.*, 2012, **68**, 336–339.

[26] C. L. Liu, K. H. Chang, C. C. Hu and W. C. Wen, *J. Power Sources*, 2012, **217**, 184-192.

[27] G. Park, L. Bartolome, K. G. Lee, S. J. Lee, D. H. Kim and T. J. Park, *Nanoscale*, 2012, **4**, 3879–3885.

[28] I. Nam, N. D. Kim, G. P. Kim, J. S. Park and J. Yi, *J. Power Sources*, 2013, **244**, 56-62.

[29] W. Hmmners, *Jam. Chem. Soc.*, 1958, **80**, 1339.

[30] L. Shahriary and A. Athawale, *International Journal of Renewable Energy and Environmental Engineering*, 2014, **02**, 58–63.

[31] Y. Z. Wu, S. Q. Liu, H. Y. Wang, X. W. Wang, X. Zhang and G. H. Jin, *Electrochim. Acta*, 2013, **90**, 210–218.

[32] J. W. Lee, A. S. Hall, J. D. Kim and T. E. Mallouk, *Chem. Mater.*, 2012, **24**, 1158−1164.

[33] B. G. S. Raj, R. N. R. Ramprasad, A. M. Asiri, J. J. Wu and S. Anandan, *Electrochim. Acta*, 2015, **156**, 127–137.

[34] G. W. Li, B. M. Zhang, F. Yu, A. A. Novakova, M. S. Krivenkov, T. Y. Kiseleva, L. Chang, J. C. Rao, A. O. Polyakov, G. R. Blake, R. A. D. Groot and T. T. M. Palstra, *Chem. Mater.*, 2014, **26**, 5821−5829.

[35] A. Rahmoun, M. Loske and A. Rosin, *Energy Procedia*, 2014, **46**, 204−213.

[36] E. Barsoukov and J. R. Macdonald, Impedance Spectroscopy Theory, Experiment, and Applications, A John Wiley & Sons Inc Publication, Hoboken, 2005.

[37] L. X. Yang, Y. Liang, H. Chen, Y. F. Meng and W. Jiang, *Mater. Res. Bull.*, 2009, **44**, 1753–1759.

[38] D. P. Dubal, D. S. Dhawale, R. R. Salunkhe, S. M. Pawar, V. J. Fulari and C. D. Lokhande, *J. Alloys Compd.*, 2009, **484**, 218–221.

[39] D. P. Dubal, D. S. Dhawale, R. R. Salunkhe, V. J. Fulari and C. D. Lokhande, *J.*

Alloys Compd., 2010, **497**, 166–170.

Figure captions

Fig.1. (a) ~ (c), (e) HRTEM images, (d) XRD spectra of GO, rGO and Mn_3O_4/graphene, (f) SAED pattern of Mn_3O_4/graphene and (g) TEM images of pristine graphene.

Fig.2. SEM images of (a), (b) Mn_3O_4, (c), (d) Mn_3O_4/graphene and (e) the grain distribution of Mn_3O_4/graphene.

Fig.3. (a) FT-IR spectrum of graphite oxide (GO) and Mn_3O_4/graphene (MGC) and (b) Raman curves of graphite oxide (GO), reduced graphene oxide (rGO) and Mn_3O_4/graphene (MGC).

Fig.4. XPS spectra for (a) survey spectra, (b) the C1s regions, (c) the Mn3s regions, (d) the Mn2p regions and TGA profile of (e) Mn_3O_4 and (f) Mn_3O_4/graphene nanocomposites.

Fig.5. (a) The comparison of discharge/charge capacity between Mn_3O_4 and Mn_3O_4/graphene electrode at the current density of 60 mA/g for 100 times, (b) Galvanostatic discharge/charge profiles of Mn_3O_4 and Mn_3O_4/graphene electrode at a current density of 200 mA/g , (c) The rate capacity of Mn_3O_4 and Mn_3O_4/graphene electrode.

Fig.6. Nyquist plots of Mn_3O_4 and Mn_3O_4/graphene electrodes.

Fig.7. Equivalent circuit used for analysis of impedance spectra of the lithium ion insertion / desertion in the intercalation electrode.

Scheme.1. The schematic for the fabrication of Mn_3O_4 on graphene oxide and the reduction of graphene oxide to graphene.

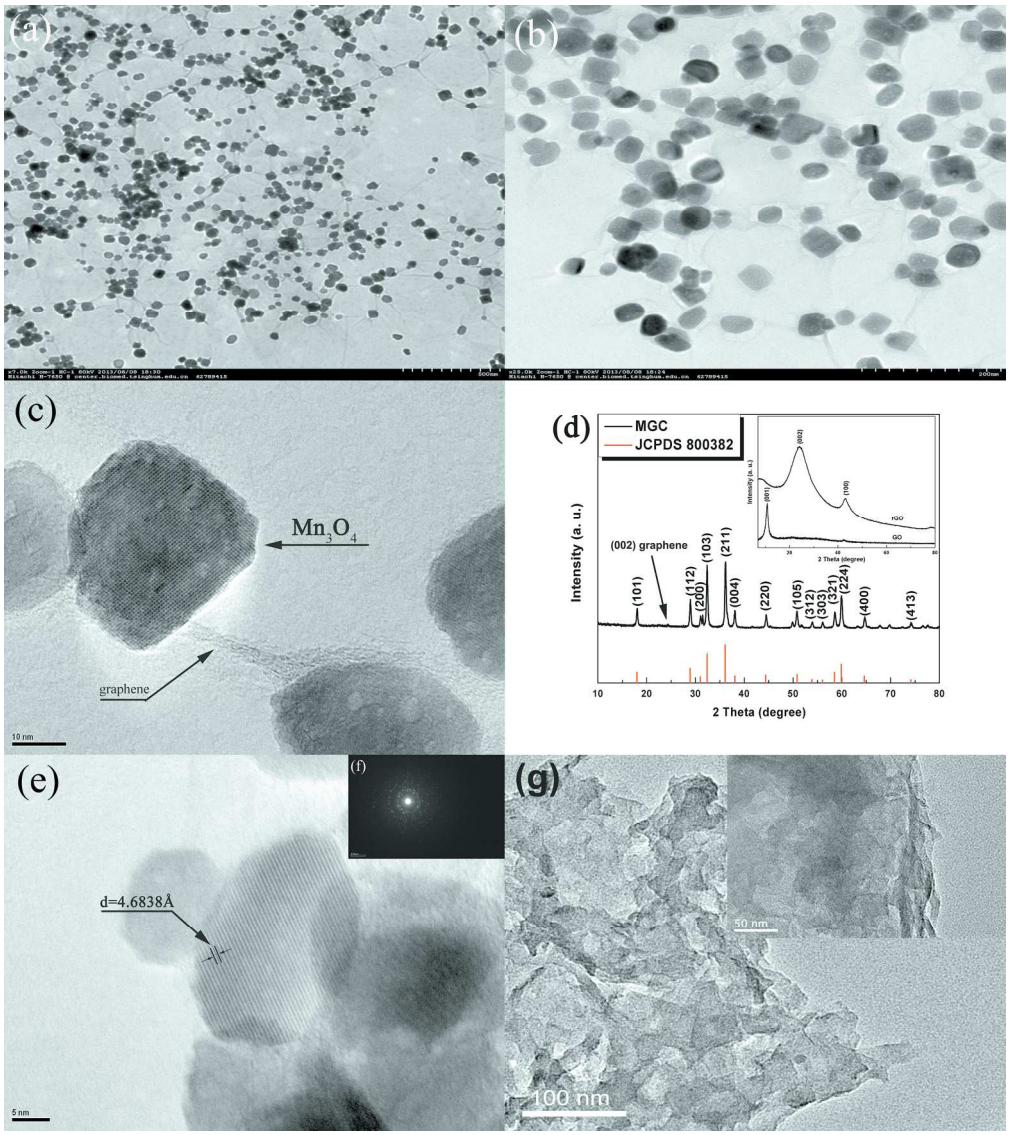

192x216mm (300 x 300 DPI)

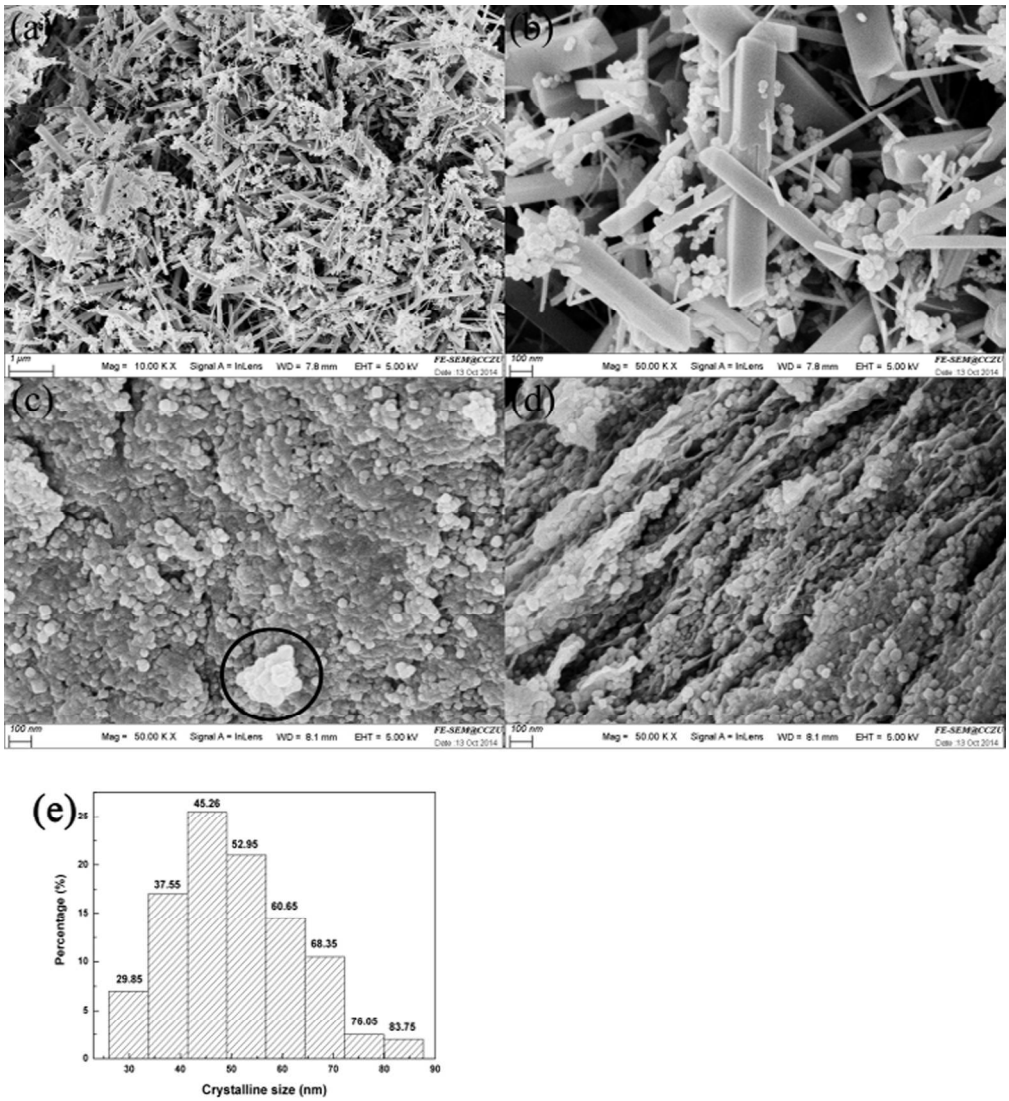

92x102mm (600 x 600 DPI)

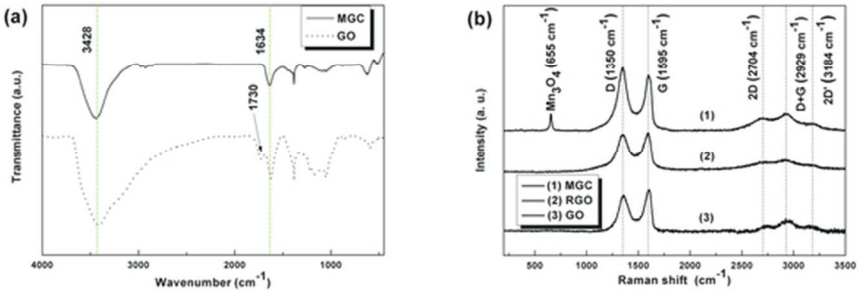

28x10mm (600 x 600 DPI)

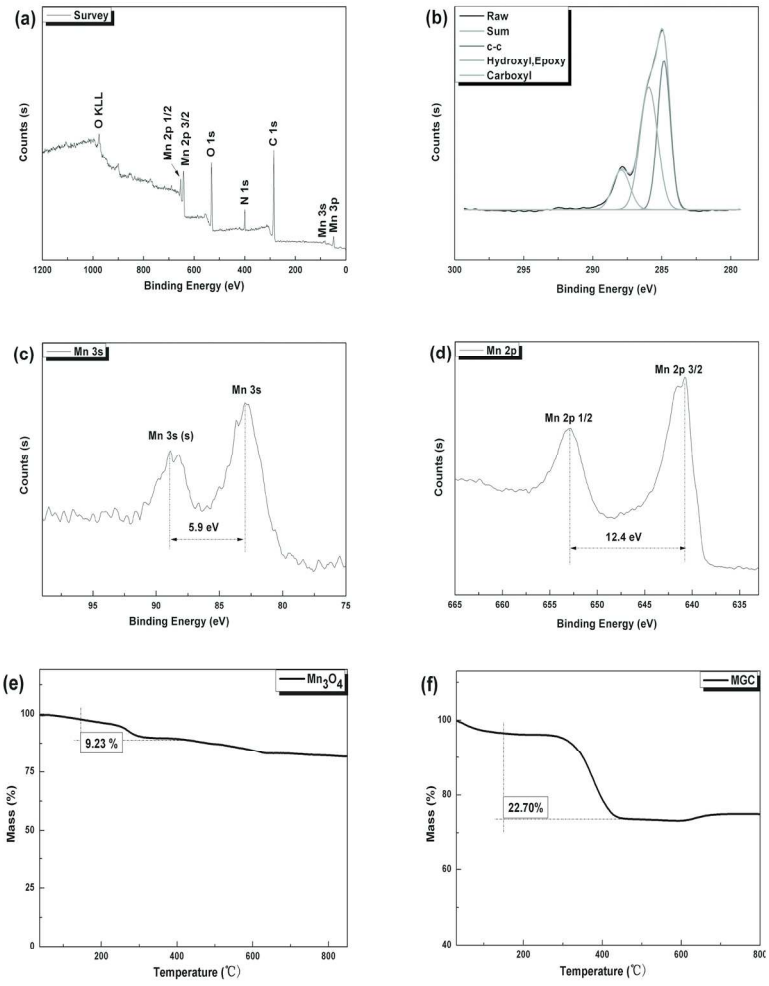

90x97mm (600 x 600 DPI)

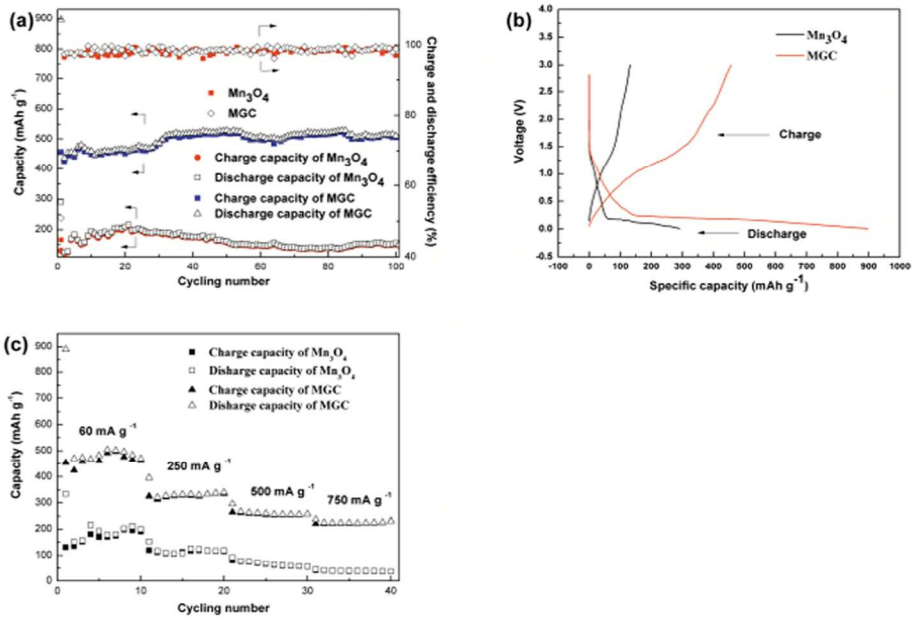

57x39mm (600 x 600 DPI)

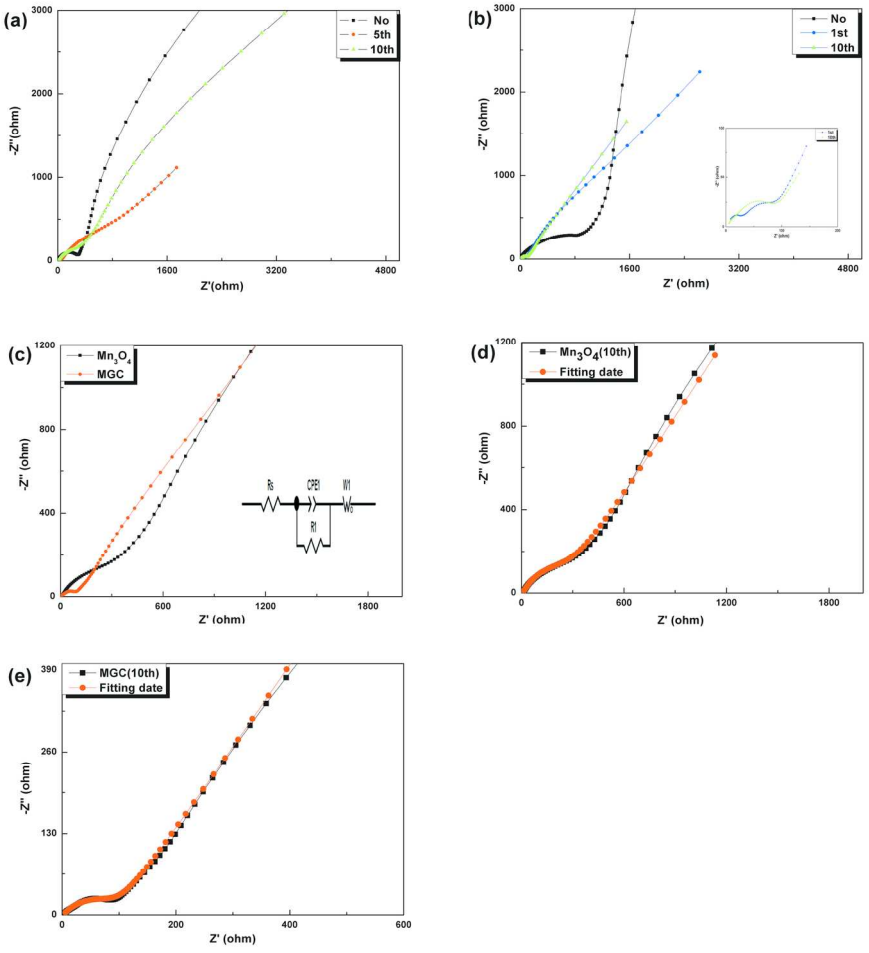

86x91mm (600 x 600 DPI)

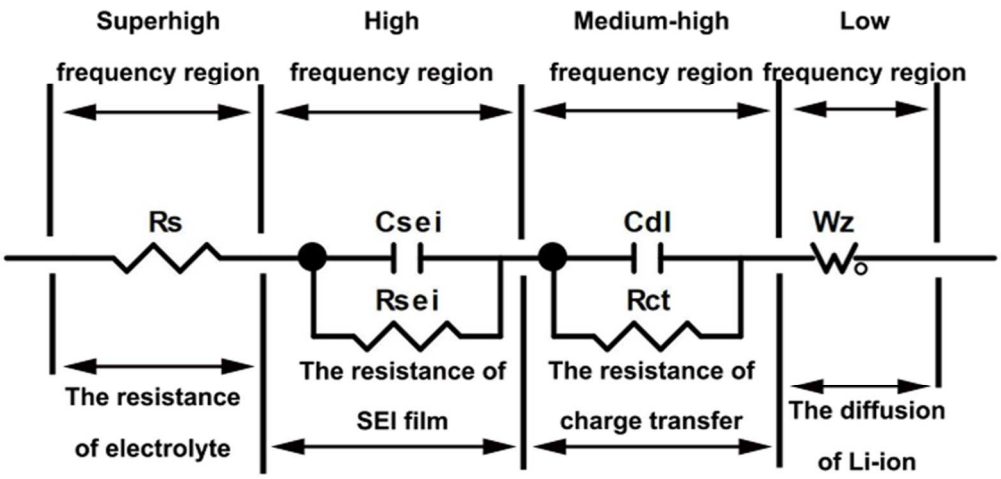

49x29mm (600 x 600 DPI)

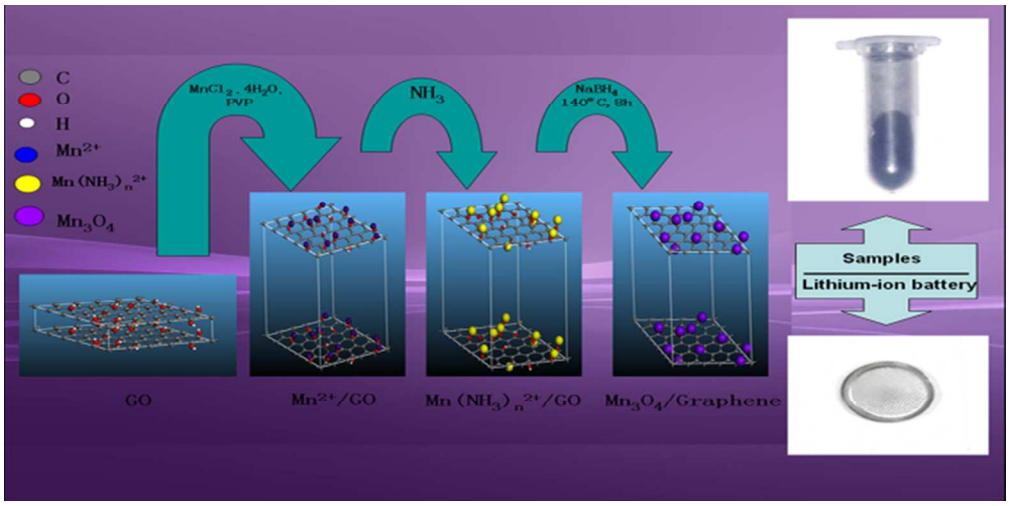

41x20mm (600 x 600 DPI)